

Probing invisible neutrino decay with the first six detection units of KM3NeT/ORCA

S. Aiello^a A. Albert^{b,be} A. R. Alhebsi^c M. Alshamsi^d S. Alves Garre^e A. Ambrosone^{g,f}
 F. Ameli^h M. Andreⁱ L. Aphecetche^j M. Ardid^k S. Ardid^k J. Aublin^l F. Badaracco^{n,m}
 L. Bailly-Salins^o Z. Bardačová^{q,p} B. Baret^l A. Bariego-Quintana^e Y. Becherini^l
 M. Bendahman^f F. Benfenati Gualandi^{s,r} M. Benhassi^{t,f} M. Bennani^u D. M. Benoit^v
 E. Berbee^w V. Bertin^d S. Biagi^x M. Boettcher^y D. Bonanno^x A. B. Bouasla^{bf}
 J. Boumaaza^z M. Bouta^d M. Bouwhuis^w C. Bozza^{aa,f} R. M. Bozza^{g,f} H. Brânzaș^{ab}
 F. Bretaudeau^j M. Breuhaus^d R. Bruijn^{ac,w} J. Brunner^d R. Bruno^a E. Buis^{ad,w}
 R. Buompane^{t,f} J. Busto^d B. Caiffiⁿ D. Calvo^e A. Capone^{h,ae} F. Carenini^{s,r}
 V. Carretero^{ac,w,e,1} T. Cartraud^l P. Castaldi^{af,r} V. Cecchini^e S. Celli^{h,ae} L. Cerisy^d
 M. Chabab^{ag} A. Chen^{ah} S. Cherubini^{ai,x} T. Chiarusi^r M. Circella^{aj} R. Clark^{ak}
 R. Cocimano^x J. A. B. Coelho^l A. Coleiro^l A. Condorelli^{g,f} R. Coniglione^x P. Coyle^d
 A. Creusot^l G. Cuttone^x R. Dallier^j A. De Benedittis^f G. De Wasseige^{ak} V. Decoene^j
 P. Deguire^d I. Del Rosso^{s,r} L. S. Di Mauro^x I. Di Palma^{h,ae} A. F. Díaz^{al}
 D. Diego-Tortosa^x C. Distefano^x A. Domi^{am} C. Donzaud^l D. Dornic^d
 E. Drakopoulou^{an} D. Drouhin^{b,be} J.-G. Ducoin^d P. Duverne^l R. Dvornický^q T. Eberl^{am}
 E. Eckerová^{q,p} A. Eddymaoui^z T. van Eeden^w M. Eff^l D. van Eijk^w I. El Bojaddaini^{ao}
 S. El Hedri^l S. El Mentawi^d V. Ellajosyula^{n,m} A. Enzenhöfer^d G. Ferrara^{ai,x}
 M. D. Filipović^{ap} F. Filippini^r D. Franciotti^x L. A. Fusco^{aa,f} S. Gagliardini^{ae,h} T. Gal^{am}
 J. García Méndez^k A. Garcia Soto^e C. Gatus Oliver^w N. Geißelbrecht^{am} E. Genton^{ak}
 H. Ghaddari^{ao} L. Gialanella^{t,f} B. K. Gibson^v E. Giorgio^x I. Goos^l P. Goswami^l
 S. R. Gozzini^e R. Gracia^{am} C. Guidi^{m,n} B. Guillon^o M. Gutiérrez^{aq} C. Haack^{am}
 H. van Haren^{ar} A. Heijboer^w L. Hennig^{am} J. J. Hernández-Rey^e A. Idrissi^x
 W. Idrissi Ibsalili^f G. Illuminati^{s,r} D. Joly^d M. de Jong^{as,w} P. de Jong^{ac,w} B. J. Jung^w
 P. Kalaczyński^{bg,at} V. Kikvadze^{au} G. Kistauri^{av,au} C. Kopper^{am} A. Kouchner^{aw,l} Y. Y.
 Kovalev^{ax} L. Krupa^p V. Kueviakoe^w V. Kulikovskiyⁿ R. Kvatadze^{av} M. Labalme^o
 R. Lahmann^{am} M. Lamoureux^{ak} G. Larosa^x C. Lastoria^o J. Lazar^{ak} A. Lazo^e
 S. Le Stum^d G. Lehaut^o V. Lemaître^{ak} E. Leonora^a N. Lessing^e G. Levi^{s,r}
 M. Lindsey Clark^l F. Longhitano^a F. Magnani^d J. Majumdar^w L. Malerba^{n,m}
 F. Mamedov^p A. Manfreda^f A. Manousakis^{ay} M. Marconi^{m,n} A. Margiotta^{s,r}
 A. Marinelli^{g,f} C. Markou^{an} L. Martin^j M. Mastrodicasa^{ae,h} S. Mastroianni^f
 J. Mauro^{ak} K. C. K. Mehta^{az} A. Meskar^{ba} G. Miele^{g,f} P. Migliozzi^f E. Migneco^x
 M. L. Mitsou^{t,f} C. M. Mollo^f L. Morales-Gallegos^{t,f} A. Moussa^{ao} I. Mozun Mateo^o
 R. Muller^r M. R. Musone^{t,f} M. Musumeci^x S. Navas^{aq} A. Nayerhoda^{aj} C. A. Nicolau^h
 B. Nkosi^{ah} B. Ó Fearraighⁿ V. Oliviero^{g,f} A. Orlando^x E. Oukacha^l D. Paesani^x
 J. Palacios González^e G. Papalashvili^{aj,au} V. Parisi^{m,n} A. Parmar^o E. J. Pastor Gomez^e
 C. Pastore^{aj} A. M. Păun^{ab} G. E. Păvălaș^{ab} S. Peña Martínez^l M. Perrin-Terrin^d

¹Corresponding author

V. Pestel^o R. Pestes^l P. Piattelli^x A. Plavin^{ax,bh} C. Poirè^{aa,f} V. Popa^{†2ab} T. Pradier^b
J. Prado^e S. Pulvirenti^x C.A. Quiroz-Rangel^k N. Randazzo^a A. Ratnani^{bb}
S. Razzaque^{bc} I. C. Rea^f D. Real^e G. Riccobene^x A. Romanov^{m,n,o} E. Ros^{ax} A. Šaina^e
F. Salesa Greus^e D. F. E. Samtleben^{as,w} A. Sánchez Losa^e S. Sanfilippo^x
M. Sanguineti^{m,n} D. Santonocito^x P. Sapienza^x M. Scarnera^{ak,l} J. Schnabel^{am}
J. Schumann^{am} H. M. Schutte^y J. Seneca^w N. Sennan^{ao} P. Sevlè^{ak} I. Sgura^{aj}
R. Shanidze^{au} A. Sharma^l Y. Shitov^p F. Šimkovic^q A. Simonelli^f A. Sinopoulou^a
B. Spisso^f M. Spurio^{s,r} D. Stavropoulos^{an} I. Štek^p M. Taiuti^{m,n} G. Takadze^{au}
Y. Tayalati^{z,bb} H. Thiersen^y S. Thoudam^c I. Tosta e Melo^{a,ai} B. Trocmé^l
V. Tsourapis^{an} A. Tudorache^{h,ae} E. Tzamariudaki^{an} A. Ukleja^{ba} A. Vacheret^o
V. Valsecchi^x V. Van Elewyck^{aw,l} G. Vannoye^{d,n} G. Vasileiadis^{bd} F. Vazquez de Sola^w
A. Veutro^{h,ae} S. Viola^x D. Vivolo^{t,f} A. van Vliet^c E. de Wolf^{ac,w} I. Lhenry-Yvon^l
S. Zavatarelliⁿ A. Zegarelli^{h,ae} D. Zito^x J. D. Zornoza^e J. Zúñiga^e N. Zywučka^y

^aINFN, Sezione di Catania, (INFN-CT) Via Santa Sofia 64, Catania, 95123 Italy

^bUniversité de Strasbourg, CNRS, IPHC UMR 7178, F-67000 Strasbourg, France

^cKhalifa University of Science and Technology, Department of Physics, PO Box 127788, Abu Dhabi, United Arab Emirates

^dAix Marseille Univ, CNRS/IN2P3, CPPM, Marseille, France

^eIFIC - Instituto de Física Corpuscular (CSIC - Universitat de València), c/Catedrático José Beltrán, 2, 46980 Paterna, Valencia, Spain

^fINFN, Sezione di Napoli, Complesso Universitario di Monte S. Angelo, Via Cintia ed. G, Napoli, 80126 Italy

^gUniversità di Napoli “Federico II”, Dip. Scienze Fisiche “E. Pancini”, Complesso Universitario di Monte S. Angelo, Via Cintia ed. G, Napoli, 80126 Italy

^hINFN, Sezione di Roma, Piazzale Aldo Moro 2, Roma, 00185 Italy

ⁱUniversitat Politècnica de Catalunya, Laboratori d'Aplicacions Bioacústiques, Centre Tecnològic de Vilanova i la Geltrú, Avda. Rambla Exposició, s/n, Vilanova i la Geltrú, 08800 Spain

^jSubatech, IMT Atlantique, IN2P3-CNRS, Nantes Université, 4 rue Alfred Kastler - La Chantellerie, Nantes, BP 20722 44307 France

^kUniversitat Politècnica de València, Instituto de Investigación para la Gestión Integrada de las Zonas Costeras, C/ Paranimf, 1, Gandia, 46730 Spain

^lUniversité Paris Cité, CNRS, Astroparticule et Cosmologie, F-75013 Paris, France

^mUniversità di Genova, Via Dodecaneso 33, Genova, 16146 Italy

ⁿINFN, Sezione di Genova, Via Dodecaneso 33, Genova, 16146 Italy

^oLPC CAEN, Normandie Univ, ENSICAEN, UNICAEN, CNRS/IN2P3, 6 boulevard Maréchal Juin, Caen, 14050 France

^pCzech Technical University in Prague, Institute of Experimental and Applied Physics, Husova 240/5, Prague, 110 00 Czech Republic

^qComenius University in Bratislava, Department of Nuclear Physics and Biophysics, Mlynska dolina F1, Bratislava, 842 48 Slovak Republic

^rINFN, Sezione di Bologna, v.le C. Berti-Pichat, 6/2, Bologna, 40127 Italy

^sUniversità di Bologna, Dipartimento di Fisica e Astronomia, v.le C. Berti-Pichat, 6/2, Bologna, 40127 Italy

^{2†} Deceased

- ^t *Università degli Studi della Campania "Luigi Vanvitelli", Dipartimento di Matematica e Fisica, viale Lincoln 5, Caserta, 81100 Italy*
- ^u *LPC, Campus des Cézeaux 24, avenue des Landais BP 80026, Aubière Cedex, 63171 France*
- ^v *E. A. Milne Centre for Astrophysics, University of Hull, Hull, HU6 7RX, United Kingdom*
- ^w *Nikhef, National Institute for Subatomic Physics, PO Box 41882, Amsterdam, 1009 DB Netherlands*
- ^x *INFN, Laboratori Nazionali del Sud, (LNS) Via S. Sofia 62, Catania, 95123 Italy*
- ^y *North-West University, Centre for Space Research, Private Bag X6001, Potchefstroom, 2520 South Africa*
- ^z *University Mohammed V in Rabat, Faculty of Sciences, 4 av. Ibn Battouta, B.P. 1014, R.P. 10000 Rabat, Morocco*
- ^{aa} *Università di Salerno e INFN Gruppo Collegato di Salerno, Dipartimento di Fisica, Via Giovanni Paolo II 132, Fisciano, 84084 Italy*
- ^{ab} *Institute of Space Science, INFLPR subsidiary, 409 Atomistilor St., Magurele, Ilfov, 077125 Romania*
- ^{ac} *University of Amsterdam, Institute of Physics/IHEF, PO Box 94216, Amsterdam, 1090 GE Netherlands*
- ^{ad} *TNO, Technical Sciences, PO Box 155, Delft, 2600 AD Netherlands*
- ^{ae} *Università La Sapienza, Dipartimento di Fisica, Piazzale Aldo Moro 2, Roma, 00185 Italy*
- ^{af} *Università di Bologna, Dipartimento di Ingegneria dell'Energia Elettrica e dell'Informazione "Guglielmo Marconi", Via dell'Università 50, Cesena, 47521 Italia*
- ^{ag} *Cadi Ayyad University, Physics Department, Faculty of Science Semlalia, Av. My Abdellah, P.O.B. 2390, Marrakech, 40000 Morocco*
- ^{ah} *University of the Witwatersrand, School of Physics, Private Bag 3, Johannesburg, Wits 2050 South Africa*
- ^{ai} *Università di Catania, Dipartimento di Fisica e Astronomia "Ettore Majorana", (INFN-CT) Via Santa Sofia 64, Catania, 95123 Italy*
- ^{aj} *INFN, Sezione di Bari, via Orabona, 4, Bari, 70125 Italy*
- ^{ak} *UCLouvain, Centre for Cosmology, Particle Physics and Phenomenology, Chemin du Cyclotron, 2, Louvain-la-Neuve, 1348 Belgium*
- ^{al} *University of Granada, Department of Computer Engineering, Automation and Robotics / CITIC, 18071 Granada, Spain*
- ^{am} *Friedrich-Alexander-Universität Erlangen-Nürnberg (FAU), Erlangen Centre for Astroparticle Physics, Nikolaus-Fiebiger-Straße 2, 91058 Erlangen, Germany*
- ^{an} *NCSR Demokritos, Institute of Nuclear and Particle Physics, Ag. Paraskevi Attikis, Athens, 15310 Greece*
- ^{ao} *University Mohammed I, Faculty of Sciences, BV Mohammed VI, B.P. 717, R.P. 60000 Oujda, Morocco*
- ^{ap} *Western Sydney University, School of Computing, Engineering and Mathematics, Locked Bag 1797, Penrith, NSW 2751 Australia*
- ^{aq} *University of Granada, Dpto. de Física Teórica y del Cosmos & C.A.F.P.E., 18071 Granada, Spain*
- ^{ar} *NIOZ (Royal Netherlands Institute for Sea Research), PO Box 59, Den Burg, Texel, 1790 AB, the Netherlands*
- ^{as} *Leiden University, Leiden Institute of Physics, PO Box 9504, Leiden, 2300 RA Netherlands*

^{at} AGH University of Krakow, Center of Excellence in Artificial Intelligence, Al. Mickiewicza 30, Krakow, 30-059 Poland

^{au} Tbilisi State University, Department of Physics, 3, Chavchavadze Ave., Tbilisi, 0179 Georgia

^{av} The University of Georgia, Institute of Physics, Kostava str. 77, Tbilisi, 0171 Georgia

^{aw} Institut Universitaire de France, 1 rue Descartes, Paris, 75005 France

^{ax} Max-Planck-Institut für Radioastronomie, Auf dem Hügel 69, 53121 Bonn, Germany

^{ay} University of Sharjah, Sharjah Academy for Astronomy, Space Sciences, and Technology, University Campus - POB 27272, Sharjah, - United Arab Emirates

^{az} AGH University of Krakow, Faculty of Physics and Applied Computer Science, Reymonta 19, Krakow, 30-059 Poland

^{ba} National Centre for Nuclear Research, 02-093 Warsaw, Poland

^{bb} School of Applied and Engineering Physics, Mohammed VI Polytechnic University, Ben Guerir, 43150, Morocco

^{bc} University of Johannesburg, Department Physics, PO Box 524, Auckland Park, 2006 South Africa

^{bd} Laboratoire Univers et Particules de Montpellier, Place Eugène Bataillon - CC 72, Montpellier Cédex 05, 34095 France

^{be} Université de Haute Alsace, rue des Frères Lumière, 68093 Mulhouse Cedex, France

^{bf} Université Badji Mokhtar, Département de Physique, Faculté des Sciences, Laboratoire de Physique des Rayonnements, B. P. 12, Annaba, 23000 Algeria

^{bg} AstroCeNT, Nicolaus Copernicus Astronomical Center, Polish Academy of Sciences, Rektorska 4, Warsaw, 00-614 Poland

^{bh} Harvard University, Black Hole Initiative, 20 Garden Street, Cambridge, MA 02138 USA

E-mail: vcarrretero@km3net.de, km3net-pc@km3net.de

ABSTRACT: In the era of precision measurements of neutrino oscillation parameters, it is necessary for experiments to disentangle discrepancies that may indicate physics beyond the Standard Model in the neutrino sector. KM3NeT/ORCA is a water Cherenkov neutrino detector under construction and anchored at the bottom of the Mediterranean Sea. The detector is designed to study the oscillations of atmospheric neutrinos and determine the neutrino mass ordering. This paper focuses on the initial configuration of ORCA, referred to as ORCA6, which comprises six out of the foreseen 115 detection units of photosensors. A high-purity neutrino sample was extracted during 2020 and 2021, corresponding to an exposure of 433 kton-years. This sample is analysed following a binned log-likelihood approach to search for invisible neutrino decay, in a three-flavour neutrino oscillation scenario, where the third neutrino mass state ν_3 decays into an invisible state, e.g. a sterile neutrino. The resulting best fit of the invisible neutrino decay parameter is $\alpha_3 = 0.92^{+1.08}_{-0.57} \times 10^{-4} \text{ eV}^2$, corresponding to a scenario with θ_{23} in the second octant and normal neutrino mass ordering. The results are consistent with the Standard Model, within a 2.1σ interval.

Contents

| | | |
|----------|---|-----------|
| 1 | Introduction | 1 |
| 2 | Invisible decay effects on neutrino oscillations | 3 |
| 3 | The KM3NeT/ORCA detector | 6 |
| 4 | Data sample and event selection | 7 |
| 5 | Analysis method | 9 |
| 6 | Results | 11 |
| 7 | Conclusions | 18 |
| 8 | Acknowledgements | 18 |

1 Introduction

The discovery of neutrino oscillations at the turn of the century, implying the existence of at least two non-zero neutrino mass states, constituted the first landmark observation of a deviation from the Standard Model (SM) of particle physics [1]. While most of the parameters that govern the oscillation mechanism are now measured with good precision [2], some of them remain uncertain, such as the Dirac CP phase (δ), the octant of the mixing angle θ_{23} , and the neutrino mass ordering, which is either normal (NO: $m_1 < m_2 \ll m_3$) or inverted (IO: $m_3 \ll m_1 < m_2$). Other signatures of physics beyond the Standard Model (BSM) may exist in the neutrino sector and are actively searched for, one of them being the possibility of neutrino decay.

The concept of neutrino decay was introduced in 1972 as a potential solution for the solar neutrino problem [3], although subsequent investigations revealed that the neutrino decay scenario cannot account for the observed deficit of solar neutrinos [4]. Massive neutrinos may have radiative decay channels, e.g. $\nu_j \rightarrow \nu_i + \gamma$ [5, 6]; however the expected lifetimes for such processes are too long to be tested experimentally [7, 8]. A variety of BSM theoretical scenarios have also been proposed, typically allowing for the decay of (Majorana or Dirac) neutrinos into a lighter fermion state and some BSM particles; we refer the reader to ref. [9] for a brief overview of such, and more exotic, models.

Neutrino decays can be phenomenologically classified into visible or invisible channels, depending on the nature of the decay products and their detectability [10]. Invisible decay occurs when the decay products remain undetected, either because they are sterile neutrinos or because they have such low energy that they fall below the detection threshold of

the experiment. In contrast, visible decay involves either the emission of photons or the production of lower-energy active neutrinos, which retain enough energy to be detected through interactions. In this paper, we primarily focus on the scenario of invisible neutrino decay, regardless of the specific decay model or products. This is mainly motivated by the fact that the expected decay signal from the non-sterile channels in the atmospheric neutrino telescopes is expected to contribute only negligibly to the event rate at the lowest detectable energy threshold because of a sharply-decreasing atmospheric neutrino flux with energy.

The invisible decay of relativistic neutrinos can be described by a depletion factor $D = e^{-\frac{m_i L}{\tau_i E}}$, where τ_i is the rest-frame lifetime of the neutrino mass state m_i , representing the fraction of neutrinos with energy E that survive after travelling a distance L . The invisible neutrino decay is then characterised by the parameter $\alpha_i = \frac{m_i}{\tau_i}$, which is expressed in natural units of eV^2 . In principle, any of the neutrino mass eigenstates ν_1, ν_2 and ν_3 having non-zero mass could potentially lead to invisible decays.

Currently, the most stringent, albeit model-dependent, limits on neutrino decay come from cosmology [11]. Other studies have shown that the decays of ν_1 and ν_2 are strongly restricted by data from the supernova SN1987A [12] and solar neutrino experiments [13]. While the decay of ν_3 remains an open possibility, ongoing accelerator, atmospheric, and reactor neutrino experiments have not yet observed any evidence of this phenomenon. Existing constraints on the neutrino lifetime based upon invisible decays are generally weaker, mainly arising from combined fits using data from T2K and NO ν A [14] ($\alpha_3 < 2.4 \times 10^{-4} \text{ eV}^2$ at 90% CL), T2K and MINOS [15] ($\alpha_3 < 2.9 \times 10^{-4} \text{ eV}^2$ at 90% CL), T2K, MINOS and NO ν A [16] ($\alpha_3 < 2.7 \times 10^{-5} \text{ eV}^2$ at 90% CL) and SK, K2K and MINOS [17] ($\alpha_3 < 2.3 \times 10^{-6} \text{ eV}^2$ at 90% CL). Constraints on neutrino decay can also be inferred from astrophysical neutrino data. In particular, the tension observed between different classes of events in IceCube data has been reduced by $\sim 3\sigma$ when considering the invisible neutrino decay hypothesis [18]. For a more comprehensive exploration of the current status and future prospects concerning neutrino decay, both invisible and visible, readers can refer to the review in ref. [9].

Due to their sensitivity in a large range of neutrino energies and propagation distances, atmospheric neutrino experiments are particularly appealing to investigate the effects of neutrino decay. Large-volume Cherenkov detectors, such as the KM3NeT/ORCA underwater neutrino telescope [19], offer the possibility to detect atmospheric neutrinos in the GeV to TeV range, which are an excellent probe for this kind of BSM effects that depend on the L/E ratio. The potential of the complete ORCA detector for probing the invisible decay model using such atmospheric neutrinos has been studied in ref. [20], showing that it could improve current limits on α_3 by up to two orders of magnitude.

In this paper, the invisible neutrino decay of ν_3 is probed with the data sample collected with ORCA6, an early subarray of the KM3NeT/ORCA detector, in the period from January 2020 to November 2021. Section 2 briefly discusses the effects of invisible decay on neutrino oscillations. Section 3 presents the KM3NeT/ORCA neutrino detector. Section 4 summarises the event selection, reconstruction and classification procedures. The analysis

method is described in section 5, and results are presented and discussed in section 6.

2 Invisible decay effects on neutrino oscillations

In the standard, 3-neutrino oscillation framework, flavour eigenstates ν_β ($\beta = e, \mu, \tau$) are linearly related to the mass eigenstates ν_i ($i = 1, 2, 3$): $\nu_\beta = \sum_{i=1}^3 U_{\beta i}^* \nu_i$, where the $U_{\beta i}$ are the elements of the Pontecorvo-Maki-Nakagawa-Sakata (PMNS) mixing matrix [21, 22], which can be parametrised in terms of three real mixing angles θ_{ij} ($i < j$) and one complex phase δ accounting for possible CP-violating effects. In the case of atmospheric neutrinos crossing the Earth, coherent scattering on electrons along the path of the neutrino modifies the oscillation probabilities. The main effect is an amplification of the transition probabilities ($\nu_\mu \leftrightarrow \nu_e$) in the resonance region (around 3 – 8 GeV) [23].

The Hamiltonian that describes the propagation of a neutrino through matter, incorporating the effect of invisible decay, can be written as:

$$H_{\text{Total}} = \frac{1}{2E} (H_0 + H_D + H_M), \quad (2.1)$$

where E is the neutrino energy, H_0 represents the Hamiltonian in vacuum, H_M encompasses the effects of coherent scattering on electrons along the path of the neutrino, and H_D accounts for neutrino decay. In the flavour eigenstate basis, the Hamiltonian responsible for oscillations reads:

$$H_{\text{Total}} = \frac{1}{2E} \left[U \begin{pmatrix} 0 & 0 & 0 \\ 0 & \Delta m_{21}^2 & 0 \\ 0 & 0 & \Delta m_{31}^2 \end{pmatrix} U^\dagger + U \begin{pmatrix} 0 & 0 & 0 \\ 0 & 0 & 0 \\ 0 & 0 & -i\alpha_3 \end{pmatrix} U^\dagger \right] + \begin{pmatrix} V & 0 & 0 \\ 0 & 0 & 0 \\ 0 & 0 & 0 \end{pmatrix}, \quad (2.2)$$

with U being the PMNS matrix, $V = \pm\sqrt{2}N_e G_F$ the matter potential, N_e the electron density in matter and G_F the Fermi constant.

The introduction of H_D thus essentially leads to a shift in the mass splitting, from Δm_{31}^2 to $\Delta m_{31}^2 - i\alpha_3$, becoming a complex number. Neutrino decay induces a global reduction in the neutrino flavour oscillation probabilities and introduces a damping effect that reduces the amplitude of the oscillatory terms [24, 25].

The influence of neutrino decay on the oscillation patterns of Earth-crossing neutrinos is illustrated in figure 1 for a specific neutrino path length and different values of the α_3 parameter. Neutrino oscillation probabilities are computed with the OscProb software [26] and the Preliminary Reference Earth Model [27] is used for the density profile of the Earth's interior. The effects of decay due to α_3 are more pronounced in channels related to the muon flavour, primarily because ν_3 contributes more to ν_μ compared to ν_e . In vacuum, the neutrino decay affects most significantly the $P_{\mu\mu}$ channel, regardless of the mass ordering. However, the amplification of the transition probabilities $\nu_\mu \leftrightarrow \nu_e$ (resp. $\bar{\nu}_\mu \leftrightarrow \bar{\nu}_e$) for the normal ordering (resp. inverted ordering) by matter effects renders these channels more sensitive to neutrino decay than in the vacuum case, especially in the energy range around the resonance. Neutrino decay also affects $\nu_\mu \leftrightarrow \nu_\tau$ transitions, with a more pronounced

effect at energies below 10 GeV. Given the kinematic threshold for tau production, this channel plays a less significant role in overall sensitivity to neutrino decay.

The parameters α_3 and θ_{23} exhibit subtle correlation effects that vary between oscillation and survival channels. The interplay between these two parameters has been extensively investigated for specific baselines in previous studies, such as refs. [16, 28–30]. Decay-induced attenuation in transition channels can be mimicked by a standard oscillation scenario with a lower θ_{23} value, while in survival channels, the effect is reversed. Figure 2 shows the muon neutrino survival and electron-to-muon transition probability for four combinations of $\theta_{23} - \alpha_3$ values and two different incoming directions. The decrease of the survival probability $P_{\mu\mu}$ at the oscillation maxima due to decay effects could be partially compensated by reducing the value of θ_{23} to the lower octant, but this would increase the probability in the energy range where matter effects are relevant. On the other hand, in the case of the transition probability $P_{e\mu}$, a higher value of θ_{23} can compensate the decrease caused by the decay effects. The change in the value of θ_{23} needed to compensate these effects depend on the cosine of the zenith angle, since the decay effects would be larger the longer the path. Therefore, this interplay degrades sensitivity to the invisible decay parameter unless the experiment can resolve a wide range of baselines and oscillation channels, allowing these effects to be disentangled [20].

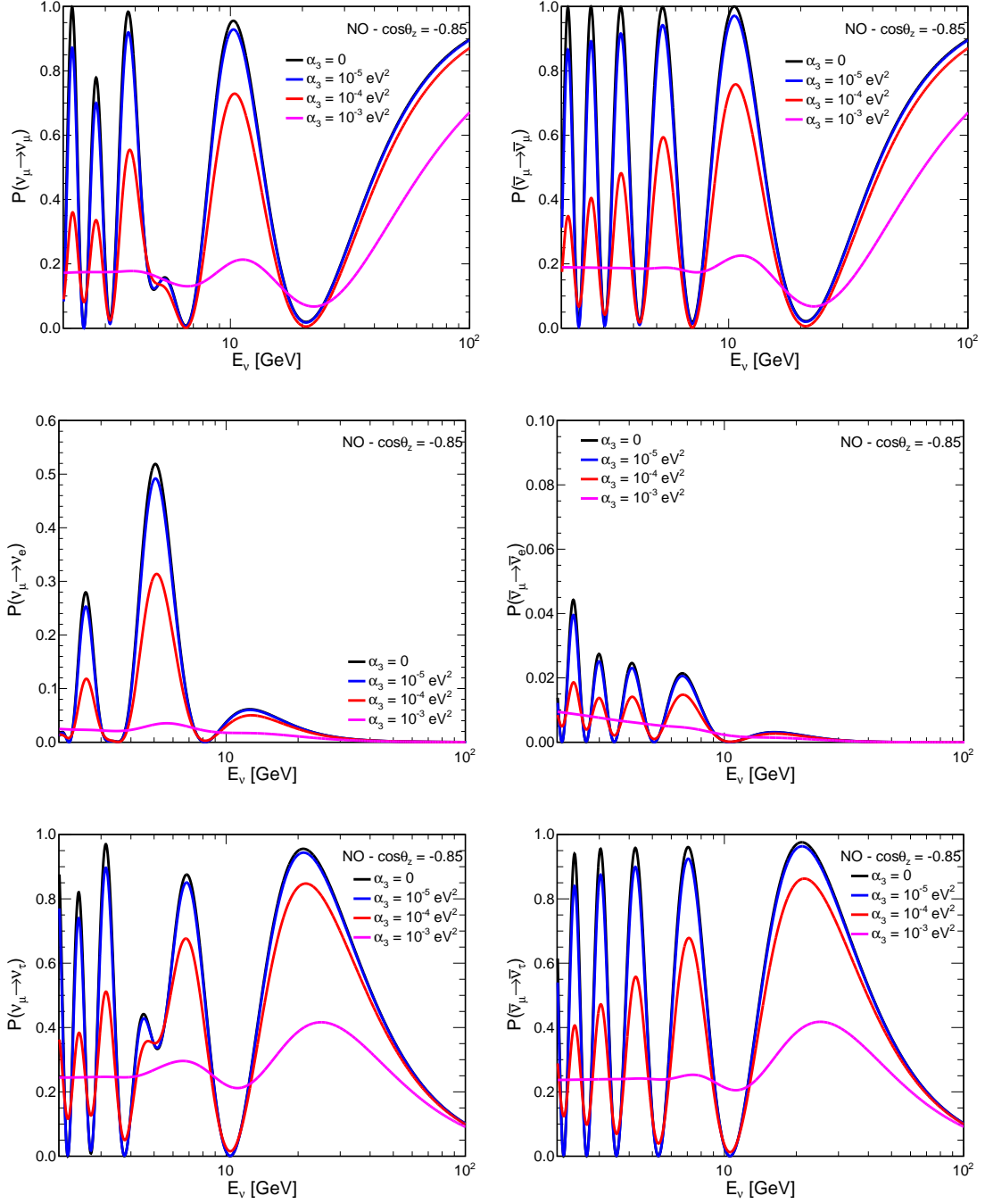


Figure 1: Probability of muon neutrino survival (top left), muon-to-electron neutrino transition (middle left), muon-to-tau neutrino transition (bottom left), muon antineutrino survival (top right), muon-to-electron antineutrino transition (middle right) and muon-to-tau antineutrino transition (bottom right) as a function of energy. All plots are obtained assuming normal ordering (NO) and $\cos\theta_z = -0.85$, where θ_z is the zenith angle associated with the neutrino trajectory, as measured from the vertical at detector location. Four values of the decay parameter are considered: $\alpha_3 = 0$ (black), $\alpha_3 = 10^{-5} \text{ eV}^2$ (blue), $\alpha_3 = 10^{-4} \text{ eV}^2$ (red) and $\alpha_3 = 10^{-3} \text{ eV}^2$ (magenta). Oscillation parameters are set to the NuFit 5.0 values with SK data [2].

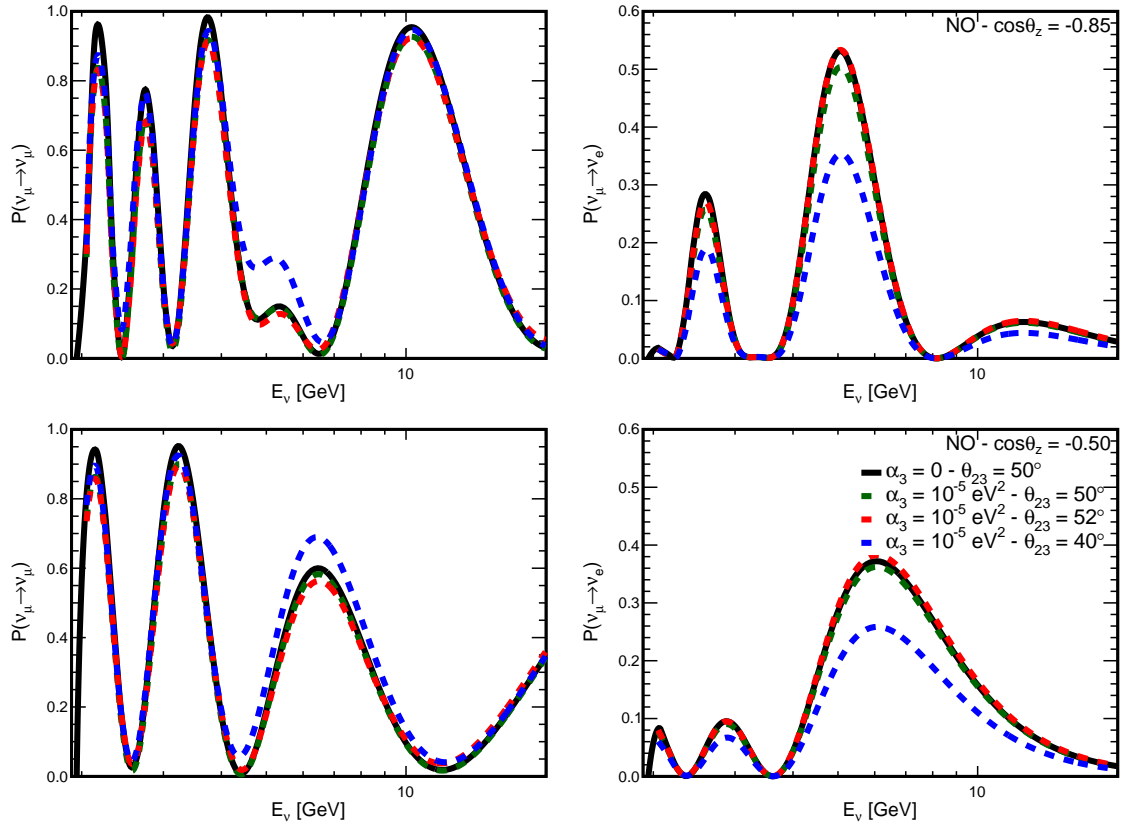


Figure 2: Muon neutrino survival (left) and electron-to-muon transition (right) probabilities as a function of energy, at a cosine of the zenith angle $\cos \theta_z = -0.85$ (top) and $\cos \theta_z = -0.50$ (bottom), assuming NO. Four cases are shown: $\alpha_3 = 0$ with $\theta_{23} = 50^\circ$ (solid black), and $\alpha_3 = 10^{-5} \text{ eV}^2$ with $\theta_{23} = 50^\circ$ (dashed green), $\theta_{23} = 52^\circ$ (dashed red), and $\theta_{23} = 40^\circ$ (dashed blue).

3 The KM3NeT/ORCA detector

The KM3NeT research infrastructure comprises two water Cherenkov detectors, called KM3NeT/ARCA and KM3NeT/ORCA, both currently under construction in the Mediterranean Sea [19]. KM3NeT/ARCA (Astroparticle Research with Cosmics in the Abyss) is located off the Sicilian coast near Capo Passero (Italy), 100 km offshore, at a depth of 3500 m. Its design is optimised for the detection of high-energy neutrinos from astrophysical sources in the TeV–PeV range. KM3NeT/ORCA (Oscillation Research with Cosmics in the Abyss) is being built near Toulon (France), 40 km offshore, at a depth of 2500 m, with the objective of measuring atmospheric neutrino oscillations in the GeV–TeV range and determining the neutrino mass ordering [31].

Both ARCA and ORCA detectors consist of arrays of detection units (DUs), which are vertical lines anchored to the seabed and supporting 18 digital optical modules (DOMs), pressure-resistant glass spheres, each equipped with 31 photomultiplier tubes (PMTs) along with the associated readout electronics and calibration instruments [32]. Upon completion,

KM3NeT/ORCA will comprise 115 detection units, with an average horizontal spacing between DUs of ~ 20 m and a vertical inter-DOM spacing of ~ 9 m, corresponding to a total instrumented volume of about 7×10^6 m³. KM3NeT/ORCA has already begun data collection during the construction phase, using increasing subsets of the planned final detector setup. During the initial phase referred to as ORCA6, the detector was operating with six out of the total 115 DUs, corresponding to an instrumented volume of about 4×10^5 m³.

The detection principle is based on the observation of Cherenkov radiation induced by relativistic charged particles originating from neutrino interactions and travelling in seawater. When PMT pulses exceed the predefined threshold, they are digitised and analysed based on their start time and duration. The data are used to reconstruct the energy and direction of the incoming neutrino. More details about the KM3NeT data acquisition and event reconstruction are provided in refs. [19, 33].

4 Data sample and event selection

This work uses data collected with the partial configuration ORCA6 of the KM3NeT/ORCA detector. In this section, the event selection and classification procedures are briefly summarised; a complete description can be found in ref. [33] since the same dataset is used.

The data analysed were collected between January 2020 and November 2021 using only period characterised by stable environmental conditions. After this selection, a total of 510 days out of the 633 days of data taking remain, corresponding to a total exposure of 433 kton-years¹. The event reconstruction considers two distinct topologies: track-like and shower-like. Track-like events arise from charged-current (CC) interactions of ν_μ and ν_τ which produce a muon in the final state. Events with electromagnetic or hadronic showers are produced by ν_e and ν_τ CC interactions, as well as neutral-current (NC) interactions of all neutrino flavours. Quality cuts based on the reconstruction filter out noise events, primarily from ⁴⁰K decays and bioluminescence [34, 35]. The analysis focuses on up-going events with the cosine of the zenith angle $\cos\theta_z < 0$ to minimise atmospheric muon background. To further distinguish neutrino-induced signals from misidentified atmospheric muons, a boosted decision tree (BDT) trained on reconstruction features is applied. The final event selection includes 5828 events, with an atmospheric muon contamination below 2%.

A second BDT is employed to classify events into track-like and shower-like categories based on their topologies. The track-like category is then divided into two subcategories: (i) a high-purity track-like class with minimal atmospheric muon contamination and an estimated ν_μ CC purity of 95% and (ii) a low-purity track-like class with less than 4% muon contamination and 90% ν_μ CC purity. The classification thresholds are optimised to maximise sensitivity to standard neutrino oscillations. In table 1, the observed and expected number of selected events per class and interaction channel are shown.

¹The exposure is computed by summing, for all the selected data taking periods, the product of the livetime by the number of active PMTs, and assuming that each active PMT instruments 108.8 tons of water (obtained by dividing the planned instrumented mass of KM3NeT/ORCA115 by the total number of PMTs in the full detector).

This division of track-like events into high- and low-purity classes enhances sensitivity to standard oscillation parameters by isolating events with superior angular resolution in the high-purity class. The energy range for events in the track classes spans from 2 to 100 GeV, while the shower class covers a broader range from 2 GeV to 1 TeV. This energy threshold for track-like events is applied to minimise the number of high-energetic tracks that pass through the detector and just leave a small fraction of their energy in it. The track energy is essentially estimated from the measured track length. Due to the limited size of the detector the algorithm provides a constantly lower energy measurement for neutrino energies above 50 GeV as most tracks at these energies deposit only a fraction of their total energy within the detector.

KM3NeT/ORCA6, 433 kton-years

| Channel | High Purity Tracks | Low Purity Tracks | Showers | Total |
|---------------------|--------------------|-------------------|---------|--------|
| ν_μ CC | 1166.2 | 1202.9 | 639.6 | 3008.7 |
| $\bar{\nu}_\mu$ CC | 607.3 | 605.6 | 217.8 | 1430.7 |
| ν_e CC | 40.2 | 69.4 | 457.7 | 567.3 |
| $\bar{\nu}_e$ CC | 16.7 | 26.9 | 190.6 | 234.2 |
| ν_τ CC | 14.6 | 13.8 | 95.8 | 124.2 |
| $\bar{\nu}_\tau$ CC | 6.6 | 6.0 | 37.2 | 49.8 |
| ν NC | 10.4 | 18.5 | 236.3 | 265.2 |
| $\bar{\nu}$ NC | 3.2 | 5.5 | 70.2 | 78.9 |
| Atm. Muons | 4.3 | 53.3 | 13.5 | 71.1 |
| Total MC | 1869.5 | 2001.9 | 1958.7 | 5830.1 |
| Total Data | 1868 | 2002 | 1958 | 5828 |

Table 1: Number of expected events and data events passing the selection criteria per class and interaction channel compared to the total number of data events in each class for an exposure of 433 kton-year. The values correspond to the best fit which is detailed in section 5 with nuisance parameters as given in table 3.

5 Analysis method

The analysis procedure to constrain the invisible decay parameter α_3 is based on the minimisation of a binned negative log-likelihood of the 2-dimensional distribution of events in reconstructed energy E_{reco} and cosine of the zenith angle $\cos\theta_{\text{reco}}$ comparing the observed data to a model prediction [36, 37]:

$$\lambda(\alpha_3; \vec{\epsilon}) = -2 \ln L = 2 \sum_i \left[(\beta_i N_i^{\text{mod}}(\alpha_3; \vec{\epsilon}) - N_i^{\text{dat}}) + N_i^{\text{dat}} \ln \left(\frac{N_i^{\text{dat}}}{\beta_i N_i^{\text{mod}}(\alpha_3; \vec{\epsilon})} \right) \right] + \frac{(\beta_i - 1)^2}{\sigma_{\beta_i}^2} + \sum_k \left(\frac{\epsilon_k - \langle \epsilon_k \rangle}{\sigma_{\epsilon k}} \right)^2, \quad (5.1)$$

where N_i^{mod} and N_i^{dat} are respectively the expected and observed number of events in bin i . The vector $\vec{\epsilon}$ represents the nuisance parameters, some of them externally constrained by other experiments. This information enters the log-likelihood as a Gaussian term derived from the probability density function (PDF) of the auxiliary measurement. The mean value $\langle \epsilon_k \rangle$ and standard deviation $\sigma_{\epsilon k}$ are the parameters used to define these PDFs. The coefficients β_i are normally distributed with uncertainties σ_i , which account for the statistical uncertainties arising from limited Monte Carlo statistics, following the Barlow-Beeston light approach [33, 38, 39].

The number of expected events is computed using the KM3NeT package Swim [40], which combines the atmospheric neutrino flux (HONDA 2014 at the Frejus site without mountain over the detector for solar minima [41]), neutrino oscillation probabilities (OscProb package [26]) and the detector response weighted by the respective neutrino-nucleon

CC and NC cross sections (GENIE [42, 43]). The detector response is simulated with Monte Carlo events by mapping the expected rate at a given bin of reconstructed energy and reconstructed cosine of the zenith angle to the corresponding bins of true energy and true cosine of the zenith angle. Neutrino events in KM3NeT/ORCA are generated with gSeaGen [43] and atmospheric muons are generated with MUPAGE [44, 45]. Cherenkov photons induced by charged particles are propagated to the PMTs using the KM3NeT package KM3Sim [46]. To speed up the simulation of light propagation in the case of high-energy particles, a custom KM3NeT package based on precomputed tables of PDFs of the light arrival time is used. The optical backgrounds due to the PMT dark count rate and to the decay of ^{40}K present in seawater are included through a KM3NeT package which also simulates the digitised output of PMT responses and the readout. The simulated events then follow the same triggering and reconstruction chain as described in section 3 for real data.

Those oscillation parameters for which KM3NeT/ORCA has no sensitivity are fixed to NuFit 5.0 including SK data values and shown in table 2. The nuisance parameters considered in this analysis can be cast into 3 categories: *normalisation factors*, *flux shape systematics* and the *absolute energy scale* of the detector. The *normalisation factors* aim to account for uncertainties in the cross sections and event selection efficiency and are applied to scale respectively the overall amount of events, f_{all} , the High Purity Tracks f_{HPT} and Shower f_{S} events, the NC events, f_{NC} , the τ CC events, $f_{\tau\text{CC}}$, the atmospheric muon events, f_{μ} and the high-energy events simulated with a different propagation software f_{HE} . The f_{HE} normalisation factor is introduced to take into account the different assumptions on light propagation made by the two light propagation software packages used. A scaling is therefore applied for NC events with true energy above 100 GeV and for CC events with true energy above 500 GeV. The *flux shape systematics* aim at modelling uncertainties in the neutrino flux by altering the ratio of up-going to horizontally-going neutrinos, δ_{θ} , the spectral index δ_{γ} , the ratio of ν_{μ} to $\bar{\nu}_{\mu}$, $s_{\mu\bar{\mu}}$, the ratio of ν_e to $\bar{\nu}_e$, $s_{e\bar{e}}$, and the ratio of ν_e to ν_{μ} , $s_{e\mu}$. The *absolute energy scale* of the detector E_s is implemented to account for uncertainties in the water properties (light absorption and scattering) and in PMT efficiencies, by shifting the true energy response function. Central values and uncertainties are summarised in table 3. The normalisations of the overall amount of events f_{all} , the High Purity Track f_{HPT} and Shower f_{S} events, and the atmospheric muon events f_{μ} are fitted freely without any constraint to accommodate for uncertainties in the selection efficiency. More details on the implementation of nuisance parameters are provided in ref. [33].

| Parameter | NO |
|----------------------|------------------------------------|
| θ_{12} | 33.44° |
| θ_{13} | 8.57° |
| Δm_{21}^2 | $7.42 \times 10^{-5} \text{ eV}^2$ |
| δ_{CP} | 197° |

Table 2: The three-flavour neutrino oscillation parameters which are fixed in the analysis from NuFit 5.0 [2] for normal ordering including SK data.

6 Results

The best fit is obtained by minimising the negative log-likelihood ratio (equation 5.1) using 8 starting points, $\theta_{23} = \{40^\circ, 50^\circ\}$, $\Delta m_{31}^2 = \{2.517 \times 10^{-3}, -2.428 \times 10^{-3}\} \text{ eV}^2$ and $E_s = \{0.95, 1.05\}$. In each fit, the parameter space is restricted to the corresponding θ_{23} octant, mass ordering and energy scale below/above one to avoid local minima.

After performing the full minimisation of equation (5.1) the observed log-likelihood ratio λ is found to be 489.3. To assess the goodness-of-fit, a set of 2000 pseudo-experiments are generated assuming NuFit 5.0 values, $\alpha_3 = 0$ and the nuisance parameters at their nominal values. The log-likelihood ratio $\lambda_{\text{GoF}} = -2 \ln L$ is computed for each of them and the corresponding distribution is shown in figure 3. The probability of observing a λ equal or larger than the observed value is $(1.21 \pm 0.24)\%$. The uncertainty is derived by bootstrapping the 2000 pseudo-experiments, i.e. sampling the pseudo-experiments with replacement to recompute the p-value.

The best-fit value is $\alpha_3 = 0.92_{-0.57}^{+1.08} \times 10^{-4} \text{ eV}^2$, corresponding to a scenario with θ_{23} in the second octant and NO. The errors are computed via the Feldman-Cousins (FC) method [47] for 68% CL. The best-fit values of the nuisance parameters, along with their post-fit uncertainties at 68% CL are shown in table 3 assuming Wilks' theorem [48]. The post-fit uncertainties are computed by profiling each of them as a parameter of interest.

| Parameter | CV \pm uncert. | Std. Best Fit | Decay Best Fit | Post-fit uncert. |
|---|-------------------|---------------|----------------|------------------|
| f_{all} | 1.00 | 1.11 | 1.35 | $-0.20/+0.25$ |
| f_{HPT} | 1.00 | 0.92 | 0.92 | $-0.04/+0.04$ |
| f_S | 1.00 | 0.92 | 0.88 | $-0.06/+0.06$ |
| f_{HE} | 1.0 ± 0.5 | 1.59 | 1.81 | $-0.32/+0.35$ |
| f_μ | 1.00 | 0.51 | 0.25 | $-0.25/+0.35$ |
| $f_{\tau CC}$ | 1.00 ± 0.20 | 0.92 | 0.96 | $-0.19/+0.19$ |
| f_{NC} | 1.00 ± 0.20 | 0.86 | 0.89 | $-0.19/+0.19$ |
| $s_{\mu\bar{\mu}}$ | 0.00 ± 0.05 | 0.00 | 0.00 | $-0.05/+0.05$ |
| $s_{e\bar{e}}$ | 0.00 ± 0.07 | 0.01 | 0.01 | $-0.07/+0.07$ |
| $s_{\mu e}$ | 0.00 ± 0.02 | -0.004 | -0.004 | $-0.020/+0.020$ |
| δ_γ | 0.0 ± 0.3 | -0.019 | -0.075 | $-0.035/+0.04$ |
| δ_θ | 0.000 ± 0.020 | -0.005 | 0.004 | $-0.020/+0.020$ |
| E_s | 1.00 ± 0.09 | 1.03 | 0.98 | $-0.08/+0.10$ |
| $\theta_{23} [^\circ]$ | 49.2 | 45.5 | 46.2 | $-4.0/+4.0$ |
| $\Delta m_{31}^2 [\times 10^{-3} \text{ eV}^2]$ | 2.52 | 2.18 | 2.15 | $-0.25/+0.28$ |

Table 3: Nuisance and oscillation parameters considered in this analysis. The second column provides the central value and uncertainty of the Gaussian prior entering the log-likelihood ratio calculation. The third, fourth and fifth columns correspond respectively to the best-fit value assuming standard oscillation hypothesis, the best-fit value assuming decay scenario and the corresponding post-fit uncertainty at 68% CL as obtained from the fit of ORCA6 data to α_3 .

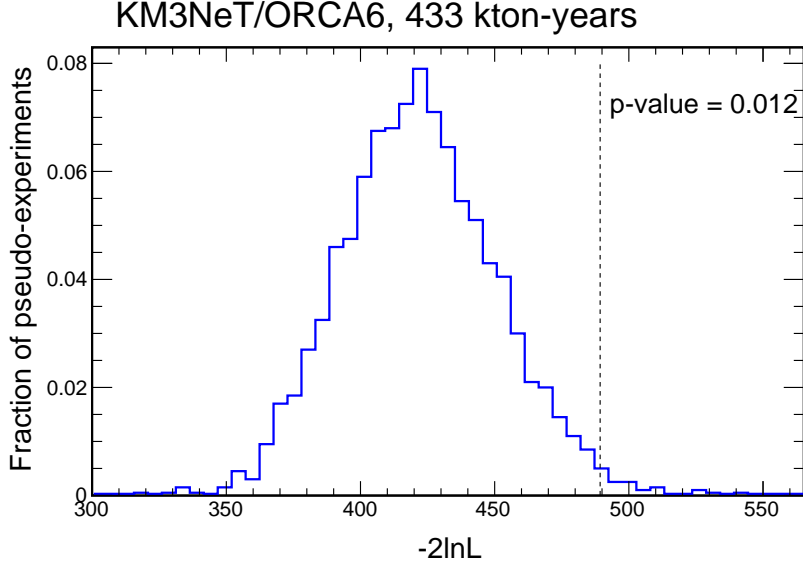


Figure 3: Distribution of λ values from 2000 pseudo-experiments used to carry out the goodness-of-fit test. The vertical line indicates the observed value of λ corresponding to the best fit to the data.

The allowed region at 90% CL for both the mixing angle θ_{23} and the invisible decay parameter α_3 is shown in figure 4, with the best-fit value indicated with a dot. The contour is derived assuming Wilks’ theorem due to computing constraints. The shape illustrates the interplay between both parameters discussed in section 2: the allowed range for α_3 is larger in the first octant region. While the current sensitivity of ORCA6 is insufficient to disentangle the θ_{23} octant, this parameter is expected to be determined at 90% CL within 3 years of operation of the full ORCA detector [20], leading to a stronger constraint on α_3 .

In order to compute Feldman-Cousins corrections to the parameter uncertainties, a set of 2000 pseudo-experiments is generated for several testing points along the profile. The results compared to the expectation from Wilks’ theorem can be seen in figure 5. The decrease of Feldman-Cousins threshold values for $\alpha_3 \rightarrow 0$ reflects the fact that the validity conditions of Wilks’ theorem are not met due to the presence of boundaries in the parameter space [49].

The difference in the likelihood of the best fit to the standard oscillation hypothesis is $\Delta\lambda_{\text{obs}} = 2.8$. The corresponding p-value is computed by simulating pseudo-experiments using as true parameter values the NuFit v5.0 best fit and computing the log-likelihood ratio $\Delta\lambda = -2(\log L_{SM} - \log L_D)$ between the Standard Model (SM) hypothesis ($\alpha_3 = 0$) and the invisible neutrino decay (D) hypothesis (α_3 free). The distribution of the log-likelihood ratio is shown in figure 6, together with the value observed from ORCA6 data analysis. The probability of getting $\Delta\lambda$ equal or higher than $\Delta\lambda_{\text{obs}}$ is $(3.9 \pm 0.4)\%$, corresponding to 2.1σ .

In figure 7, the ORCA6 result is compared with the ones obtained from combined fits using long-baseline and atmospheric neutrino data (see table 4). The data best-fit and

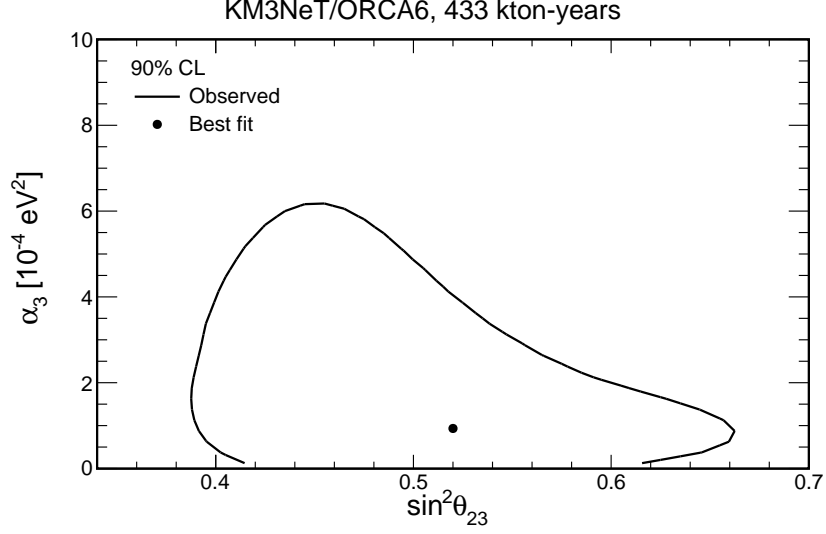


Figure 4: Allowed region at 90% CL obtained from ORCA6 data for the $\theta_{23} - \alpha_3$ parameters. The best-fit value is indicated with a dot.

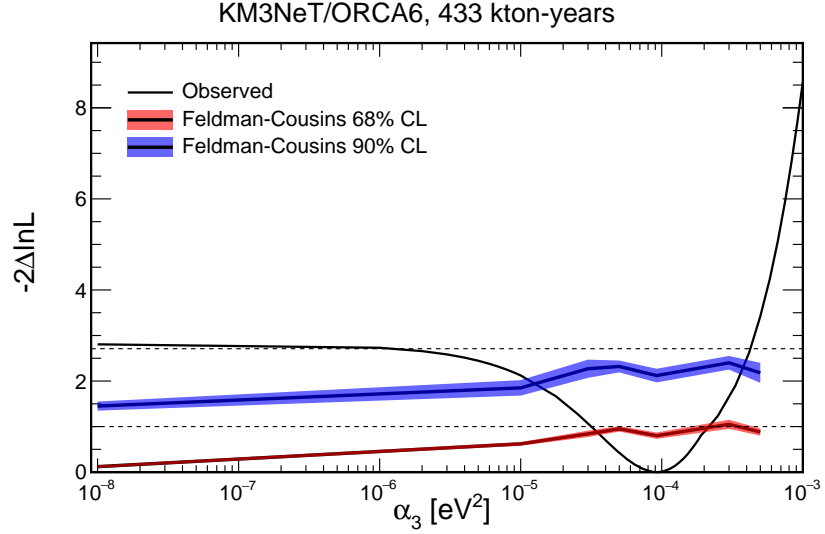


Figure 5: Profiled log-likelihood ratio of the invisible decay parameter, α_3 . The black line represents the observed result. Horizontal dashed lines represent the 68% and 90% CL thresholds assuming Wilks' theorem, while the red and blue lines show respectively the 68% and 90% Feldman-Cousins CL. The uncertainty bands are the standard deviation with respect to the CLs derived by sampling the pseudo-experiments with replacement.

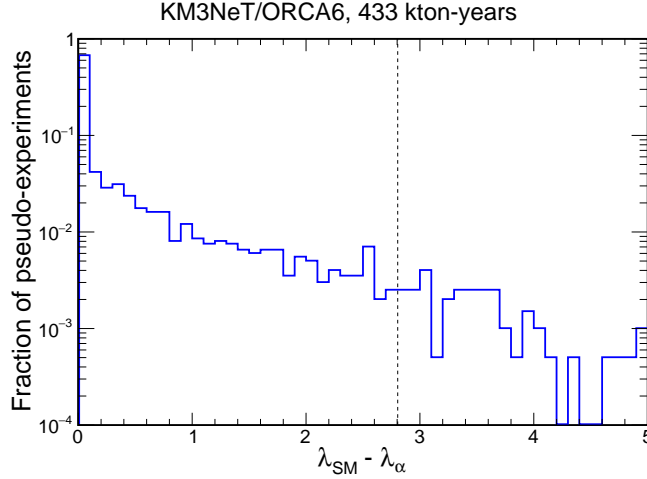


Figure 6: Distribution of the test statistic $\Delta\lambda$, obtained from a set of 2000 pseudo-experiments generated assuming as true NuFit v5.0 values and $\alpha_3 = 0$. The vertical line indicates the observed test statistic value.

intervals are in the same order of magnitude as those of combined fits with long baseline data, T2K+NO ν A (red) [14] and T2K+MINOS (magenta) [15] and one order of magnitude weaker than the combination of T2K+MINOS+NO ν A (blue) [16]. Note that for the combination of SK, K2K and MINOS data (green) [17], a two-flavour approximation is applied and matter effects are neglected, so that a complete treatment may relax the second minimum. Future accelerator experiments, such as DUNE [50], MOMENT [51], ESSnuSB [28] and T2HKK [29], as well as reactor experiments like JUNO [52], and atmospheric neutrino experiments like INO [53], are expected to provide an improved sensitivity to this parameter.

The ORCA6 event distributions for each of the three event classes are presented in figure 8 as a function of the reconstructed L/E ratio. In each plot, the data are compared to the standard oscillation best fit, the invisible decay best fit and to an extreme decay case ($\alpha_3 = 1.1 \times 10^{-3} \text{ eV}^2$), using the nuisance parameters the best-fit values to the decay hypothesis. The underfluctuation at large L/E values in the High Purity Track class is compatible with the decay hypothesis, but no such clear decrease is visible in the two other event classes.

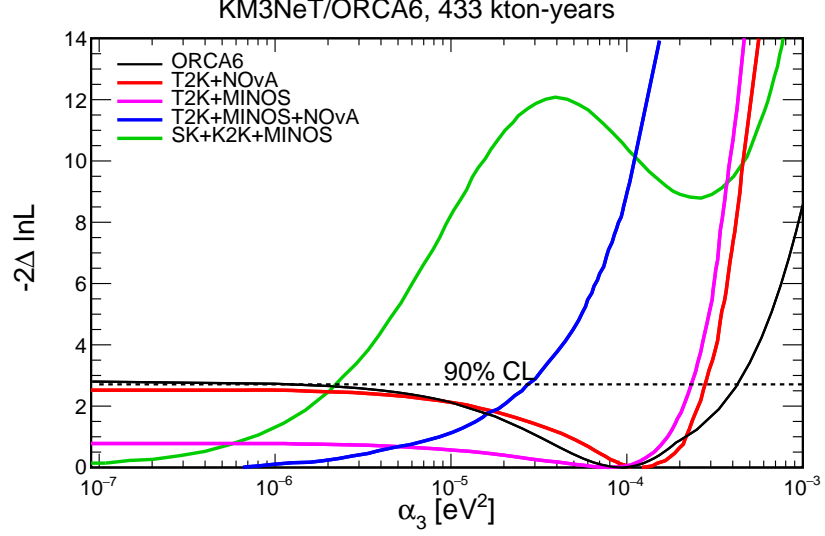


Figure 7: The observed profiled log-likelihood scan (black) compared with combined fits using data from: T2K+NO ν A (red) [14], T2K+MINOS (magenta) [15], T2K+MINOS+NO ν A (blue) [16] and SK+K2K+MINOS (green) [17].

| Experiment | UL (90% CL) [10^{-6}eV^2] | Reference |
|----------------------------------|--------------------------------------|------------|
| ORCA6 (433 kton-year) | [10, 380] | this paper |
| ORCA (70 Mton-year) | 3.7 | [20] |
| T2K, NO ν A | 290 | [14] |
| T2K, MINOS | 240 | [15] |
| T2K, NO ν A, MINOS | 27 | [16] |
| K2K, MINOS, SK I+II | 2.3 | [17] |
| DUNE ($5\nu+5\bar{\nu}$) yr | 13 | [50] |
| MOMENT (10 yr) | 24 | [51] |
| ESSnuSB ($5\nu+5\bar{\nu}$) yr | 16 – 13 | [28] |
| JUNO (5 yr) | 7 | [52] |
| INO-ICAL (10 yr) | 4.4 | [53] |

Table 4: Average upper limits (ULs) at 90% CL for the decay parameter α_3 for combined fits (blue) and future experiments. 70 Mton-years of ORCA correspond to 10 years of data taking with the full detector. This ORCA6 analysis provides an interval at 90% CL after Feldman-Cousins corrections; an upper limit can be set above 96% CL.

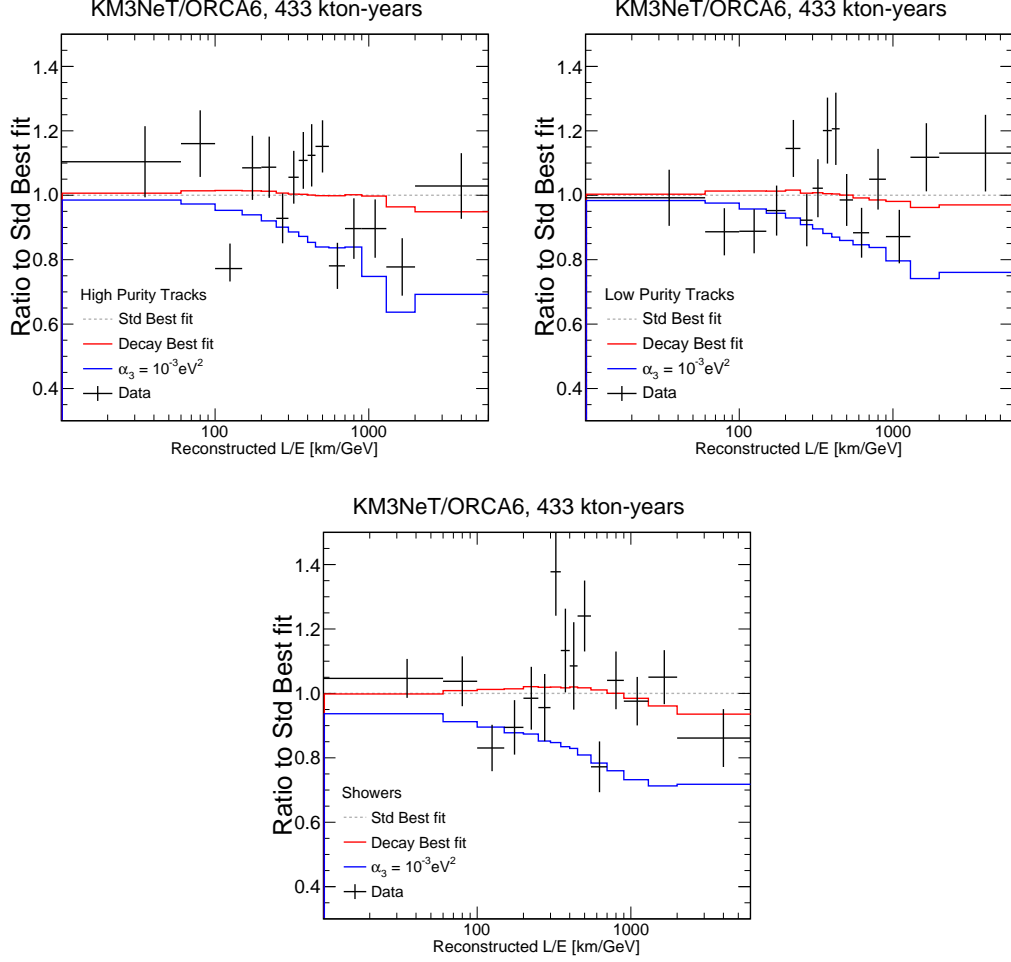


Figure 8: Ratio to the standard oscillations best fit of the reconstructed length over energy ratio, L/E , for High Purity Tracks (upper-left), Low Purity Tracks (upper-right) and Showers (bottom). The data points are shown with error bars in black, the best fit for standard oscillation hypothesis in dashed grey, the best fit assuming invisible neutrino decay in solid red, and an extreme case of decay ($\alpha_3 = 1.1 \times 10^{-3} \text{ eV}^2$) in solid blue.

The impact of each nuisance parameter on the estimation of the parameters of interest is evaluated separately, by repeating the fit while shifting the parameter value up and down by its own post-fit uncertainty. Then, the overall best-fit value of the parameter of interest is compared with the fit obtained with the "shifted" values. The difference between the nominal best fit of the parameter of interest and the "shifted" value normalised to its 1σ uncertainty is reported with boxes in figure 9. Additionally, the pulls of the best-fit (BF) nuisance parameter values with respect to the central values (CV), $(\epsilon_{\text{BF}} - \epsilon_{\text{CV}})/\sigma$, are reported as dots with error bars where σ represents their pre-fit uncertainty. Error bars for the pulls are defined as the ratio between post-fit and pre-fit uncertainties. In the case of unconstrained parameters, where no pre-fit uncertainty is set, the post-fit uncertainty is used instead.

The invisible decay parameter is mostly affected by the flux normalisation factor, the spectral index δ_γ and the horizontal-to-vertical ratio δ_θ (as the events most affected by invisible decay come from low energies and longest paths), and θ_{23} . The spectral index and the normalisation of high energy simulated events can be constrained better with the data than with the auxiliary measurements, as can be seen from the small bars. The pull in the normalisation of high-energy simulated events is expected, because the light simulation software used for high energies leads to a reduced number of selected events with respect to the simulation made with KM3Sim.

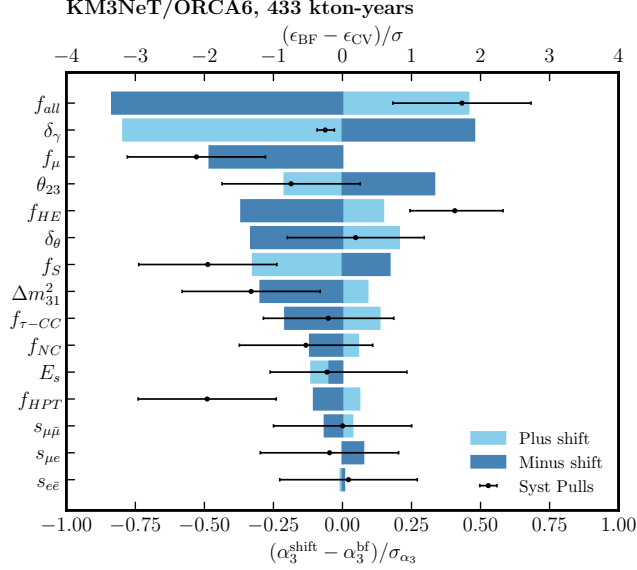


Figure 9: Impact of the nuisance parameters on α_3 evaluated by repeating the fit shifting the nuisance parameters by their post-fit uncertainties and comparing the fitted value α_3^{shift} to the best-fit value, α_3^{bf} (bottom axis). The pulls of the nuisance parameters are reported as dots (top axis) with bars representing the ratio between the post-fit uncertainties and the pre-fit uncertainties (the ratio is set to 1 for unconstrained nuisance parameters).

7 Conclusions

Based on a sample of 5828 neutrino candidates collected with the ORCA6 detector, the invisible neutrino decay parameter α_3 has been measured. The result is:

$$\alpha_3 = 0.92^{+1.08}_{-0.57} \times 10^{-4} \text{ eV}^2.$$

The corresponding likelihood ratio value is $2 \ln(L_\alpha/L_{\text{SM}}) = 2.8$ and the associated p-value is $(3.9 \pm 0.4)\%$, corresponding to 2.1σ compatibility with the Standard Model hypothesis of no neutrino decay.

The constraint on the invisible decay parameter obtained in this study is compatible with results from combined fits with data from long-baseline neutrino experiments and is of the same order of magnitude. This result indicates that even at early stages of KM3NeT/ORCA, with a small detector and limited statistics, the potential to probe scenarios beyond the Standard Model is significant.

8 Acknowledgements

The authors acknowledge the financial support of: KM3NeT-INFRADEV2 project, funded by the European Union Horizon Europe Research and Innovation Programme under grant agreement No 101079679; Funds for Scientific Research (FRS-FNRS), Francqui foundation, BAEF foundation. Czech Science Foundation (GAČR 24-12702S); Agence Nationale de la Recherche (contract ANR-15-CE31-0020), Centre National de la Recherche Scientifique (CNRS), Commission Européenne (FEDER fund and Marie Curie Program), LabEx UnivEarthS (ANR-10-LABX-0023 and ANR-18-IDEX-0001), Paris Île-de-France Region, Normandy Region (Alpha, Blue-waves and Neptune), France, The Provence-Alpes-Côte d’Azur Delegation for Research and Innovation (DRARI), the Provence-Alpes-Côte d’Azur region, the Bouches-du-Rhône Departmental Council, the Metropolis of Aix-Marseille Provence and the City of Marseille through the CPER 2021-2027 NEUMED project, The CNRS Institut National de Physique Nucléaire et de Physique des Particules (IN2P3); Shota Rustaveli National Science Foundation of Georgia (SRNSFG, FR-22-13708), Georgia; This work is part of the MuSES project which has received funding from the European Research Council (ERC) under the European Union’s Horizon 2020 Research and Innovation Programme (grant agreement No 101142396). This work was supported by the European Research Council, ERC Starting grant *MessMapp*, under contract no. 949555. The General Secretariat of Research and Innovation (GSRI), Greece; Istituto Nazionale di Fisica Nucleare (INFN) and Ministero dell’Università e della Ricerca (MUR), through PRIN 2022 program (Grant PANTHEON 2022E2J4RK, Next Generation EU) and PON R&I program (Avviso n. 424 del 28 febbraio 2018, Progetto PACK-PIR01 00021), Italy; ID-MAR project Po-Fesr Sicilian Region az. 1.5.1; A. De Benedittis, W. Idrissi Ibnsalih, M. Bendahman, A. Nayerhoda, G. Papalashvili, I. C. Rea, A. Simonelli have been supported by the Italian Ministero dell’Università e della Ricerca (MUR), Progetto CIR01

00021 (Avviso n. 2595 del 24 dicembre 2019); KM3NeT4RR MUR Project National Recovery and Resilience Plan (NRRP), Mission 4 Component 2 Investment 3.1, Funded by the European Union – NextGenerationEU, CUP I57G21000040001, Concession Decree MUR No. n. Prot. 123 del 21/06/2022; Ministry of Higher Education, Scientific Research and Innovation, Morocco, and the Arab Fund for Economic and Social Development, Kuwait; Nederlandse organisatie voor Wetenschappelijk Onderzoek (NWO), the Netherlands; The grant “AstroCeNT: Particle Astrophysics Science and Technology Centre”, carried out within the International Research Agendas programme of the Foundation for Polish Science financed by the European Union under the European Regional Development Fund; The program: “Excellence initiative-research university” for the AGH University in Krakow; The ARTIQ project: UMO-2021/01/2/ST6/00004 and ARTIQ/0004/2021; Ministry of Research, Innovation and Digitalisation, Romania; Slovak Research and Development Agency under Contract No. APVV-22-0413; Ministry of Education, Research, Development and Youth of the Slovak Republic; MCIN for PID2021-124591NB-C41, -C42, -C43 and PDC2023-145913-I00 funded by MCIN/AEI/10.13039/501100011033 and by “ERDF A way of making Europe”, for ASFAE/2022/014 and ASFAE/2022 /023 with funding from the EU NextGenerationEU (PRTR-C17.I01) and Generalitat Valenciana, for Grant AST22_6.2 with funding from Consejería de Universidad, Investigación e Innovación and Gobierno de España and European Union - NextGenerationEU, for CSIC-INFRA23013 and for CNS2023-144099, Generalitat Valenciana for CIDEAGENT/2018/034, /2019/043, /2020/049, /2021/23, for CIDEIG/2023/20, for CIPROM/2023/51 and for GRISOLIAP/2021/192 and EU for MSC/101025085, Spain; Khalifa University internal grants (ESIG-2023-008, RIG-2023-070 and RIG-2024-047), United Arab Emirates; The European Union’s Horizon 2020 Research and Innovation Programme (ChETEC-INFRA - Project no. 101008324).

References

- [1] T. Kajita, *Nobel Lecture: Discovery of atmospheric neutrino oscillations*, *Rev. Mod. Phys.* **88** (2016) 030501.
- [2] I. Esteban, M.C. Gonzalez-Garcia, M. Maltoni, T. Schwetz and A. Zhou, *The fate of hints: updated global analysis of three-flavor neutrino oscillations*, *JHEP* **09** (2020) 178.
- [3] J.N. Bahcall, N. Cabibbo and A. Yahil, *Are neutrinos stable particles?*, *Phys. Rev. Lett.* **28** (1972) 316.
- [4] A. Acker and S. Pakvasa, *Solar neutrino decay*, *Phys. Lett. B* **320** (1994) 320.
- [5] S.T. Petcov, *The Processes $\mu \rightarrow e + \gamma$, $\mu \rightarrow e + \bar{e}$, $\nu' \rightarrow \nu + \gamma$ in the Weinberg-Salam Model with Neutrino Mixing*, *Sov. J. Nucl. Phys.* **25** (1977) 340.
- [6] W. Marciano and A. Sanda, *Exotic decays of the muon and heavy leptons in gauge theories*, *Physics Letters B* **67** (1977) 303.
- [7] P.B. Pal and L. Wolfenstein, *Radiative decays of massive neutrinos*, *Phys. Rev. D* **25** (1982) 766.
- [8] J.F. Nieves, *Two-photon decays of heavy neutrinos*, *Phys. Rev. D* **28** (1983) 1664.
- [9] C.A. Argüelles et al., *Snowmass white paper: beyond the standard model effects on neutrino flavor: Submitted to the proceedings of the US community study on the future of particle physics (Snowmass 2021)*, *Eur. Phys. J. C* **83** (2023) 15.
- [10] M. Lindner, T. Ohlsson and W. Winter, *A combined treatment of neutrino decay and neutrino oscillations*, *Nuclear Physics B* **607** (2001) 326–354.
- [11] G. Barenboim, J.Z. Chen, S. Hannestad, I.M. Oldengott, T. Tram and Y.Y.Y. Wong, *Invisible neutrino decay in precision cosmology*, *JCAP* **03** (2021) 087.
- [12] J.A. Frieman, H.E. Haber and K. Freese, *Neutrino mixing, decays and supernova 1987A*, *Physics Letters B* **200** (1988) 115.
- [13] A. Bandyopadhyay, S. Choubey and S. Goswami, *Neutrino decay confronts the SNO data*, *Physics Letters B* **555** (2003) 33–42.
- [14] S. Choubey, D. Dutta and D. Pramanik, *Invisible neutrino decay in the light of NOvA and T2K data*, *JHEP* **2018** (2018) 141.
- [15] R. Gomes, A. Gomes and O. Peres, *Constraints on neutrino decay lifetime using long-baseline charged and neutral current data*, *Phys. Lett. B* **740** (2015) 345.
- [16] A. Chatterjee, S. Goswami, S. Pan and P. Thacker, *Effect of invisible neutrino decay on neutrino oscillation at long baselines*, [2411.09677](#).
- [17] M. Gonzalez-Garcia and M. Maltoni, *Status of oscillation plus decay of atmospheric and long-baseline neutrinos*, *Phys. Lett. B* **663** (2008) 405.
- [18] P.B. Denton and I. Tamborra, *Invisible neutrino decay could resolve IceCube’s track and cascade tension*, *Phys. Rev. Lett.* **121** (2018) 121802.
- [19] KM3NET collaboration, *Letter of intent for KM3NeT 2.0*, *Journal of Physics G: Nuclear and Particle Physics* **43** (2016) 084001.
- [20] KM3NET collaboration, *Probing invisible neutrino decay with KM3NeT/ORCA*, *JHEP* **04** (2023) 090.

- [21] B. Pontecorvo, *Mesonium and anti-mesonium*, *Sov. Phys. JETP* **6** (1957) 429.
- [22] Z. Maki, M. Nakagawa and S. Sakata, *Remarks on the Unified Model of Elementary Particles*, *Progress of Theoretical Physics* **28** (1962) 870.
- [23] A.Y. Smirnov, *The MSW effect and solar neutrinos*, in *10th International Workshop on Neutrino Telescopes*, pp. 23–43, 5, 2003 [[hep-ph/0305106](#)].
- [24] D.S. Chattopadhyay, K. Chakraborty, A. Dighe, S. Goswami and S.M. Lakshmi, *Neutrino propagation when mass eigenstates and decay eigenstates mismatch*, *Phys. Rev. Lett.* **129** (2022) 011802.
- [25] D.S. Chattopadhyay, K. Chakraborty, A. Dighe and S. Goswami, *Analytic treatment of 3-flavor neutrino oscillation and decay in matter*, *JHEP* **01** (2023) 051.
- [26] J. Coelho, R. Pestes, A. Domi, S. Bourret, U. Rahaman, L. Maderer et al., *joaoabcoelho/OscProb: v2.0.12*, Nov., 2023. 10.5281/zenodo.10104847.
- [27] A.M. Dziewonski and D.L. Anderson, *Preliminary reference Earth model*, *Phys. Earth Planet. Inter.* **25** (1981) 297.
- [28] S. Choubey, M. Ghosh, D. Kempe and T. Ohlsson, *Exploring invisible neutrino decay at ESSnuSB*, *JHEP* **2021** (2021) 133.
- [29] Z.F. Dey and D. Dutta, *Synergy between DUNE and T2HKK to probe invisible neutrino decay*, *JHEP* **2024** (2024) 9.
- [30] K. Chakraborty, D. Dutta, S. Goswami and D. Pramanik, *Invisible neutrino decay: first vs second oscillation maximum*, *JHEP* **2021** (2021) 91.
- [31] KM3NET collaboration, *Determining the neutrino mass ordering and oscillation parameters with KM3NeT/ORCA*, *Eur. Phys. J. C* **82** (2022) 26.
- [32] KM3NET collaboration, *The KM3NeT multi-PMT optical module*, *JINST* **17** (2022) P07038.
- [33] KM3NET collaboration, *Measurement of neutrino oscillation parameters with the first six detection units of KM3NeT/ORCA*, *JHEP* **10** (2024) 206.
- [34] ANTARES collaboration, *Long-term monitoring of the ANTARES optical module efficiencies using ^{40}K decays in sea water*, *Eur. Phys. J. C* **78** (2018) 8.
- [35] S.H. Haddock, M.A. Moline and J.F. Case, *Bioluminescence in the Sea*, *Annual Review of Marine Science* **2** (2010) 443.
- [36] R.D. Cousins, *Generalization of Chisquare Goodness-ofFit Test for Binned Data Using Saturated Models , with Application to Histograms*, 2013, <https://api.semanticscholar.org/CorpusID:5936965>.
- [37] S. Baker and R.D. Cousins, *Clarification of the use of chi square and likelihood functions in fits to histograms*, *Nucl. Instrum. Meth.* **221** (1984) 437.
- [38] R. Barlow and C. Beeston, *Fitting using finite Monte Carlo samples*, *Comput. Phys. Commun.* **77** (1993) 219.
- [39] J. Conway, *Incorporating Nuisance Parameters in Likelihoods for Multisource Spectra*, **1103.0354**.
- [40] S. Bourret, *Neutrino Oscillations and Earth Tomography with KM3NeT-ORCA*, phd thesis, Université Sorbonne Paris Cité, 2018.

- [41] M. Honda, M.S. Athar, T. Kajita, K. Kasahara and S. Midorikawa, *Atmospheric neutrino flux calculation using the NRLMSISE-00 atmospheric model*, *Phys. Rev. D* **92** (2015) 023004.
- [42] C. Andreopoulos, C. Barry, S. Dytman, H. Gallagher, T. Golan, R. Hatcher et al., *The GENIE Neutrino Monte Carlo Generator: Physics and User Manual*, *arXiv e-prints* (2015) [arXiv:1510.05494](#) [[1510.05494](#)].
- [43] KM3NET collaboration, *gSeaGen: The KM3NeT GENIE-based code for neutrino telescopes*, *Comp. Phys. Commun.* **256** (2020) 107477.
- [44] G. Carminati, M. Bazzotti, A. Margiotta and M. Spurio, *Atmospheric MUons from PArametric formulas: A Fast GEnerator for neutrino telescopes (MUPAGE)*, *Comput. Phys. Commun.* **179** (2008) 915.
- [45] Y. Becherini, A. Margiotta, M. Sioli and M. Spurio, *A Parameterisation of single and multiple muons in the deep water or ice*, *Astropart. Phys.* **25** (2006) 1.
- [46] A. Tsirigotis, A. Leisos and S. Tzamarias, *HOU Reconstruction & Simulation (HOURS): A complete simulation and reconstruction package for very large volume underwater neutrino telescopes*, *Nucl. Instrum. Meth. A* **626-627** (2011) S185.
- [47] G.J. Feldman and R.D. Cousins, *Unified approach to the classical statistical analysis of small signals*, *Physical Review D* **57** (1998) 3873.
- [48] S.S. Wilks, *The Large-Sample Distribution of the Likelihood Ratio for Testing Composite Hypotheses*, *Annals of Mathematical Statistics* **9** (1938) 60.
- [49] S. Algeri, J. Aalbers, K. Mor  and J. Conrad, *Searching for new phenomena with profile likelihood ratio tests*, *Nature Reviews Physics* **2** (2020) 1.
- [50] A. Ghoshal, A. Giarnetti and D. Meloni, *Neutrino invisible decay at DUNE: a multi-channel analysis*, *J. Phys. G: Nucl. Part. Phys.* **48** (2021) 055004.
- [51] J. Tang, T.-C. Wang and Y. Zhang, *Invisible neutrino decays at the MOMENT experiment*, *JHEP* **2019** (2019) 4.
- [52] T. Abrahao, H. Minakata, H. Nunokawa and A. Quiroga, *Constraint on neutrino decay with medium-baseline reactor neutrino oscillation experiments*, *JHEP* **2015** (2015) 1.
- [53] S. Choubey, S. Goswami, C. Gupta, S. Lakshmi and T. Thakore, *Sensitivity to neutrino decay with atmospheric neutrinos at the INO-ICAL detector*, *Phys. Rev. D* **97** (2018) 033005.